Journal of Computational Neuroscience 10, 25–45, 2001

Spike-Frequency Adaptation of a Generalized Leaky Integrate-and-Fire Model Neuron

YING-HUI LIU AND XIAO-JING WANG
Volen Center for Complex Systems and Department of Physics, Brandeis University, Waltham, MA 02454-9110
xjwang@brandeis.edu

Received ; Revised May 2, 2000; Accepted June 19, 2000

Action Editor: Bard Ermentrout

Abstract. Although spike-frequency adaptation is a commonly observed property of neurons, its functional implications are still poorly understood. In this work, using a leaky integrate-and-fire neural model that includes a Ca^{2+}-activated K^+ current (I_{AHP}), we develop a quantitative theory of adaptation temporal dynamics and compare our results with recent in vivo intracellular recordings from pyramidal cells in the cat visual cortex. Experimentally testable relations between the degree and the time constant of spike-frequency adaptation are predicted. We also contrast the I_{AHP} model with an alternative adaptation model based on a dynamical firing threshold. Possible roles of adaptation in temporal computation are explored, as a a time-delayed neuronal self-inhibition mechanism. Our results include the following: (1) given the same firing rate, the variability of interspike intervals (ISIs) is either reduced or enhanced by adaptation, depending on whether the I_{AHP} dynamics is fast or slow compared with the mean ISI in the output spike train; (2) when the inputs are Poisson-distributed (uncorrelated), adaptation generates temporal anticorrelation between ISIs, we suggest that measurement of this negative correlation provides a probe to assess the strength of I_{AHP} in vivo; (3) the forward masking effect produced by the slow dynamics of I_{AHP} is nonlinear and effective at selecting the strongest input among competing sources of input signals.

Keywords: spike-frequency adaptation, calcium-activated potassium current, integrate-and-fire neuron, variability, correlation, forward masking

1. Introduction

The evoked spike discharges of a neuron depend critically on the recent history of its electrical activity. A well-known example is the phenomenon of spike-frequency adaptation that is observed in a majority of pyramidal cells in cortical slice preparations (Connors et al., 1982; McCormick et al., 1985; Mason and Larkman, 1990; Foehring et al., 1991; Lorenzon and Foehring, 1992). However, it remains unclear is how strong the neuronal adaptation is of those cells in the intact brain and what is its role in neural computation at the single cell and network levels. A recent study by Ahmed et al. (1998) is devoted to measuring and quantifying spike-frequency adaptation of visual cortical neurons of the anesthetized cat. These authors found that the adaptation time course to a constant input is well described by a single exponential decay to steady-state, characterized by an adaptation time constant τ_{adap} and the degree of adaptation $F_{adap} =$ (initial rate—steady-state rate)/initial rate. Ahmed et al. observed that the values of τ_{adap} and F_{adap} correlate significantly with cortical depth and that superficial-layer neurons adapt more rapidly and to a higher degree than deep-layer neurons. Adaptation is fairly strong in superficial-layer neurons, with the steady-state firing rate being about only one-third of the initial firing rate. The cellular origin of these

differences between different cortical layers is not well understood.

The spike-frequency adaptation process is presumably due to the activation of several different ion channels, each with its own characteristic time constants, activation thresholds, and so on. The observations by Ahmed (1998) were made over the first 300 ms of the adaptation process, where the major changes in firing rate occur. During this period adaptation in both hippocampal and neocortical neurons is dominated by a slow Ca^{2+}-dependent K^+ current (I_{AHP}) and to a lesser extent an M-type K^+ current (Madison and Nicoll, 1984). Calcium influx is triggered by action potentials, and the rise in intracellular Ca^{2+} activates the I_{AHP} that slows the discharge rate. We have previously studied a conductance-based pyramidal neuron model endowed with an I_{AHP}, and we showed how the observations by Ahmed et al. could be accounted for in term of the membrane and calcium dynamics (Wang, 1998). The conductance-based model, however, cannot be solved analytically. In the present work, we use an integrate-and-fire (I&F) model (Lapicque, 1907, 1927; Tuckwell, 1988), which is widely utilized for large-scale network studies (Knight, 1972; Amit and Tsodyks, 1991; Somers et al., 1995; Abbott and van Vreeswijk, 1993; Hansel et al., 1998; Brunel, 2000). We generalize the I&F model to include a Ca^{2+}-activated K^+ current and carry out a thorough analytical treatment of the model. In particular, we derive τ_{adap} and F_{adap} in terms of the biophysical parameters of the model and predict experimentally testable relations between τ_{adap} and F_{adap}. Our results suggest possible explanations for the differences among neurons of different cortical layers as observed by Ahmed et al. (1998).

We also consider an alternative model where adaptation is generated by an activity-dependent dynamical firing *threshold* (Holden, 1976). In pyramidal neurons, an increase in voltage threshold has been occasionally observed experimentally in association with firing-frequency adaptation (cf., for instance, Fig. 4(B) of Mason and Larkman, 1990). It is not clear which of the two factors contribute the most to the observed physiological data of spike-frequency adaptation and how these two scenarios may be differentiated experimentally. We report that although these two adaptation models show some similarities, there are important differences that can be used to distinguish these alternative mechanisms.

We have explored possible computational implications of spike-frequency adaptation. We focused on its modulation of neuronal response to *time-varying inputs*, in contrast to previous modeling work (Douglas et al., 1995; Barkai and Hasselmo, 1994), where I_{AHP} was incorporated as a *static* gain control. Our basic observation is that the Ca^{2+}-mediated I_{AHP} subserves a time-delayed inhibition to the neuron itself, which gives rise to a number of interesting computational effects. When the input is Poisson, even in the steady state after the adaptation onset the adaptation mechanism is still operative dynamically; it affects the variability of the spike train and creates negative temporal correlations in the output. The interplay between the time constant of I_{AHP} and the mean ISI is crucial in determining how I_{AHP} affects the variability of the output spike train. Moreover, as a mechanism of temporal interaction between responses to different input signals, the I_{AHP} enables the cell to differentiate the signals and selectively respond to the strongest input amongst competing input signals (Pollack, 1988; Sobel and Tank, 1994).

2. Methods

2.1. The Leaky Integrate-and-Fire Model

For a leaky integrate-and-fire model,

$$C_m \frac{dV_m}{dt} = -g_L(V_m - V_{rest}) + C_m \Delta V \sum_i \delta(t - t_i). \tag{1}$$

If $V_m > V_{th}$, then a spike is discharged and V_m is reset to V_{reset}, C_m is the capacitance, g_L is the leak conductance, and $\sum_i \delta(t - t_i)$ represents a Poisson train of synaptic inputs with a rate λ in Hz (Stein, 1965). Each synaptic input produces a quantal excitatory postsynaptic potential of size $\Delta V = 1$ mV. Note that the delta-function description of synaptic inputs does not take into account realistic time courses of synaptic currents. However, the results presented in this article do not depend on this simplification. The average current resulting from the Poisson synaptic input is given by $I = C_m \Delta V \lambda$.

2.2. Spike-Frequency Adaptation

Spike-frequency adaptation is modeled based on the assumptions that it is produced mainly by a Ca^{2+}-gated K^+ current I_{AHP} (Madison and Nicoll, 1984).

Experiments using photolytic manipulation of Ca^{2+} suggest that the intrinsic gating of I_{AHP} is fast, thus its slow activation is due to the kinetics of the cytoplasmic Ca^{2+} concentration (Lancaster and Zucker, 1994). Let $I_{AHP} = g_{AHP}[Ca^{2+}](V - V_K)$. Each action potential generates a small amount (α) of calcium influx; hence I_{AHP} is incremented accordingly. Note that $g_{AHP}[Ca^{2+}]$ is the effective K^+ conductance and that the product αg_{AHP} is the amount of *AHP*-conductance increase by the increase of cytoplasmic Ca^{2+} concentration through a single spike. The modified integrate-and-fire model with adaptation is given by

$$C_m \frac{dV_m}{dt} = -g_L(V_m - V_{rest}) + C_m \Delta V \sum_i \delta(t - t_i) - g_{AHP}[Ca^{2+}](V_m - V_K) \quad (2)$$

$$\frac{d[Ca^{2+}]}{dt} = -\frac{[Ca^{2+}]}{\tau_{Ca}}. \quad (3)$$

$$\text{If } V_m(t) = V_{th}, \text{ then } \begin{cases} V_m \to V_{reset} \\ [Ca^{2+}] \to [Ca^{2+}] + \alpha, \end{cases} \quad (4)$$

where the $[Ca^{2+}]$ dynamics is modeled as a leaky integrator with a decay time constant τ_{Ca} (Traub, 1982). $[Ca^{2+}]$ is initially set to be 0 μM (its resting baseline is neglected). Similar models have been used previously (Treves, 1993; Stemmler et al., 1995; Troyer and Miller, 1997).

For a given neuron type, Each of the model parameters can be estimated by experimental data. In the case of cortical regular spiking pyramidal neurons: (a) $C_m = 0.5$ nF, $g_L = 0.025$ μS (the input resistance $R_{in} = 40$ MΩ) so that the time constant $\tau_m = C_m/g_L = 20$ ms, and the resting membrane potential $V_{rest} = -70$ mV (McCormick et al., 1985). (b) The firing threshold $V_{th} = -54$ mV (Mason and Larkman, 1990). (c) The slope of the f-I curve (at large I and with $g_{AHP} = 0$) is given by $1/(C_m\theta)$, where $\theta = V_{th} - V_{reset}$. We choose $V_{reset} = -60$ mV ($\theta = 6$ mV) so that the slope is about 330 Hz/nA, comparable with the primary f-I data (measured before the adaptation onset) (McCormick et al., 1985; Mason and Larkamn, 1990). (d) the $[Ca^{2+}]$ influx per spike $\alpha = 0.2$ μM, and $\tau_{Ca} = 50 - 600$ ms (Helmchen et al., 1996; Svoboda et al., 1997). (e) g_{AHP} is a parameter that is varied in simulations. Typically we used $g_{AHP} = 0.015$ mS/cm^2 (with $V_K = -80$ mV) so that the degree of adaptation is comparable with the data of Ahmed et al. (1998).

We also investigated an alternative, voltage threshold model, based on the assumption that adaptation is due to a gradual increase of the voltage firing threshold (Holden, 1976; Koch, 1999). The model obeys the following equations:

$$C_m \frac{dV_m}{dt} = -g_L(V_m - V_{rest}) + C_m \Delta V \sum_i \delta(t - t_i) \quad (5)$$

$$\frac{d\theta}{dt} = -\frac{\theta - \theta_0}{\tau_\theta}. \quad (6)$$

$$\text{If } V_m(t) = V_{th}, \text{ then } \begin{cases} V_m \to V_{reset} \\ \theta \to \theta + \alpha', \end{cases} \quad (7)$$

where, again, $\theta = V_{th} - V_{reset}$, θ is increased by $\alpha' = 0.1$ mV with each spike, and it decays back to the original value $\theta_0 = 10$ mV with a time constant $\tau_\theta = 80$ ms between spikes.

2.3. *Spike-Train Analysis*

A spike train is converted into a sequence of ISIs $\{\Delta t_1, \Delta t_2, \ldots, \Delta t_N\}$. If its mean is denoted as $< \Delta t >$, then the average firing rate is $f = 1/< \Delta t >$. The variance of ISIs is defined as

$$VAR = \frac{1}{N} \sum_{i=1}^{N} (\Delta t_i - < \Delta t >)^2, \quad (8)$$

and coefficient of variance CV as (Stein, 1967; Tuckwell, 1988; Softky and Koch, 1993; Holt et al., 1996)

$$CV = \frac{\sqrt{VAR}}{< \Delta t >}. \quad (9)$$

For spike trains that undergo frequency adaptation, both $< \Delta t >$ and CV evolve in time. We calculated their time-dependent values as follows: time is divided into bins of $dt = 1$ ms. For each trial of Poisson input, we assigned each ISI into the bin (say, $(t, t + dt)$) where the first of the spike pair occurs (the results are similar if the choice is based on the second of the spike pair). The simulation was run over many trials (typically $N = 300$), from which a collection of ISIs is accumulated for each time bin. Then the average $< \Delta t > (t)$ and $CV(t)$ are computed at that time. The mean instantaneous firing rate is $f(t) = 1/< \Delta t >(t)$.

We analyzed the temporal correlations between ISIs only in the stationary state after the average firing rate

reaches its adapted steady-state value. Let $< \Delta t >$ and *CV* be the stationary values. The correlation covariance *CORR* between consecutive ISIs is defined as

$$CORR = \frac{1}{N-1}\sum_{i=1}^{N-1}(\Delta t_i - < \Delta t >) \times (\Delta t_{i+1} - < \Delta t >), \quad (10)$$

and coefficient of correlation $CC = CORR/VAR$. Note that *CC* is between -1 and 1. For a Poisson process—in fact, for any renewal process—there is no correlation between consecutive ISIs; therefore, $CC = 0$.

Another way to visualize correlations between ISIs is to use an ISI return map, in which each Δt_{i+1} is plotted versus the preceding Δt_i. We also found it useful to plot the conditional average of Δt_{i+1} for each Δt_i. This function of Δt_i can be superimposed on the ISI return map. In fact, there is a direct connection between this function and the *CC*: if the conditional average of Δt_{i+1} is a linear function of Δt_i, then the slope of the linear curve is equal to *CC* (Wang, 1998).

The model was numerically integrated using a fourth-order Runge-Kutta method (Press et al., 1989), with time step $dt = 0.01 - 0.02$ ms.

3. Results

3.1. Dynamical Properties of Adaptation Time Course

In response to the stochastic synaptic input with a rate $\lambda = 2500$ Hz, the instantaneous firing rate of the adaptation model decreases exponentially in time from an initial firing rate to a steady-state firing rate with a characteristic time constant as shown in Fig. 1A–B. $[Ca^{2+}]$ increases up to a plateau level with the same time course (Fig. 1(C)).

Theoretically, we can derive the adaptation time constant τ_{adap} by a fast-slow variable analysis (Rinzel, 1985, 1987; Wang and Rinzel, 1995; Guckenheimer et al., 1997; Wang, 1998; Ermentrout, 1998). The method is based on the observation that the change in $[Ca^{2+}]$ is slow compared with that in V_m, so that the slower $[Ca^{2+}]$ dynamics (hence frequency adaptation) can be solved by averaging over the faster voltage subsystem. This is done in three steps. First, the slow variable $[Ca^{2+}]$ is treated as a parameter, and then Eq. (2) for the membrane potential is just a standard integrate-and-fire model, with an additional "leak current" $I_{AHP} = g_{AHP}[Ca^{2+}](V - V_K)$. This equation is solved like Eq. (1), and the firing rate f is a function of both input drive and $[Ca^{2+}]$. For sufficiently large input drive I, the f-I curve is approximately linear. As a consequence, we found that the dependence of f on $[Ca^{2+}]$ could also be well approximated by a linear relation,

$$f([Ca^{2+}]) = f_{init} - G_f[Ca^{2+}], \quad (11)$$

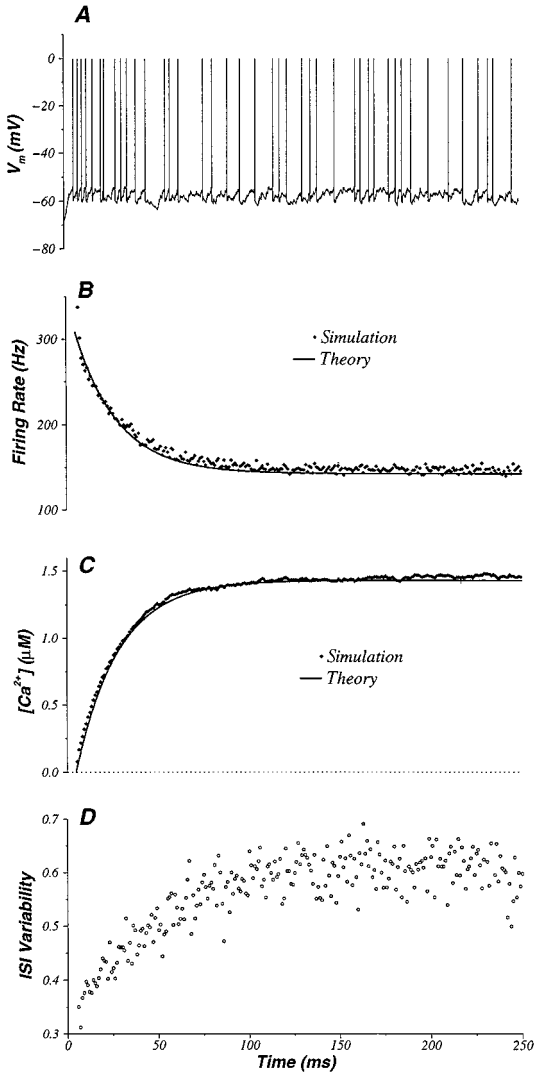

Figure 1. Simulation results of adaptation time course for I_{AHP} model. **A:** Adaptation in response to Poisson synaptic inputs with rate $\lambda = 2500$ Hz. **B:** The trial-averaged instantaneous firing rate decreases in time exponentially with a characteristic time constant τ_{adap}. **C:** The intracellular $[Ca^{2+}]$ level builds up with the same time course. **D:** The adaptation process is also associated with an increase of *ISI* variability in time. ($\tau_{Ca} = 50$ ms.)

where G_f is a derived constant (Appendix A). In the second step, after averaging over the fast variable V_m, the equation for the slow variable $[Ca^{2+}]$ becomes

$$\begin{aligned}\frac{d[Ca^{2+}]}{dt} &= \alpha f - \frac{[Ca^{2+}]}{\tau_{Ca}} \\ &= \alpha f_{init} - (G_{adap} + 1/\tau_{Ca})[Ca^{2+}],\end{aligned} \tag{12}$$

where $G_{adap} = \alpha G_f$. Solving this linear equation yields

$$[Ca^{2+}]\,(t) = [Ca^{2+}]_{ss}\,(1 - \exp(-t/\tau_{adap})), \tag{13}$$

with $1/\tau_{adap} = G_{adap} + 1/\tau_{Ca}$. Finally, in the third step, by inserting $[Ca^{2+}](t)$ into Eq. (11), we obtain the time course for the spike-frequency adaptation:

$$\begin{aligned}f(t) &= f_{init} - G_f([Ca^{2+}]_{ss}(1 - \exp(-t/\tau_{adap}))) \\ &= f_{ss} + (f_{init} - f_{ss})\exp(-t/\tau_{adap}).\end{aligned} \tag{14}$$

A detailed mathematical derivation using this procedure is given in Appendix A.

This way, we were able to obtain an analytical expression for the adaptation time constant

$$\begin{aligned}\tau_{adap} &= \left[\frac{1}{\tau_{Ca}} + G_{adap}\right]^{-1}, \ \textit{where} \\ G_{adap} &= \frac{\alpha g_{AHP}}{C_m}\left(\frac{V_{reset} - V_K}{\theta} + \frac{1}{2}\right).\end{aligned} \tag{15}$$

Therefore, τ_{adap} is a simple function of τ_{Ca} (the $[Ca^{2+}]$ decay time constant) and αg_{AHP} (the increment of K^+ conductance per spike). This result shows that τ_{adap} is always smaller than the calcium decay time constant τ_{Ca}. When calcium dynamics is very slow (τ_{Ca} very large), the adaptation process may still be fast (with small τ_{adap}) because the dominant term in the equation is controlled by αg_{AHP}. For example, with our reference parameter set $G_{adap} = 0.023$. From Eq. (15) we have $\tau_{adap} = 23,\ 35.7,\ 41.7$ ms, if $\tau_{Ca} = 50,\ 200,\ 1000$ ms, respectively.

Thus, the $[Ca^{2+}]$ and spike-frequency adaptation time course are given by Eqs. (13) and (14) with $\tau_{adap} = 23$ ms, the steady state $[Ca^{2+}] = 1.43\ \mu$M, the initial firing rate $f_{init} = 308$ Hz, and the final steady-state rate $f_{ss} = 143$ Hz. The theoretically derived time courses are superimposed on the simulation data in Fig. 1B–C for the instantaneous firing rate and intracellular $[Ca^{2+}]$. The agreement between the analytical and numerical results is remarkable, given that with $\tau_{Ca} = 50$ ms and $\tau_m = 20$ ms in the parameter set the assumed separation of fast-slow time scales is quite crude. The input amplitude and other parameters were adjusted so that the range of frequency adaptation was comparable with in vivo recording data from cat visual cortex by Ahmed et al. (1998, Figs. 4–5). The good fit by a single exponential to the adaptation time course in the experimental data is similar to the model.

We also calculated the coefficient of variation for the ISIs as a function of time CV(t). The output ISI variability increases at the onset of adaptation as shown in Fig. 1D, with a time course similar to that of the decrease in firing rate. This monotonic increase in the variability at the onset of adaptation is a characteristic of the I_{AHP} mechanism and will be further discussed later in this article.

3.2. *Degree of Adaptation*

The degree of adaptation (F_{adap}) is defined as the ratio of the change in the firing rate during adaptation ($f_{init} - f_{ss}$) to the initial firing rate before adaptation f_{init}:

$$F_{adap} \equiv \frac{f_{init} - f_{ss}}{f_{init}}. \tag{16}$$

With our parameter set, $F_{adap} \sim 54\%$.

F_{adap} depends on two factors: the strength of adaptation (determined by the product αg_{AHP}, and α is fixed in the following discussion) and the Ca^{2+} kinetics (determined by τ_{Ca}). We investigated the effects of these two factors on F_{adap} separately. First, we vary the adaptation conductance g_{AHP}, while fixing the calcium kinetics (τ_{Ca}). With a large g_{AHP}, we expect a strong adaptation (large F_{adap}) and the steady state to be reached quickly (small τ_{adap}). Conversely, if g_{AHP} is small, we expect the adaptation effect to be negligible ($F_{adap} \to 0$), and since the firing rate is almost constant in time, $\tau_{adap} \to \tau_{Ca}$ according to Eq. (12). In other words, F_{adap} and τ_{adap} are predicted to vary in the opposite manner. Indeed, it can be proved that with a fixed Ca^{2+} kinetics, a simple negative linear relation exists between F_{adap} and τ_{adap} (Appendix A):

$$F_{adap} = 1 - \frac{\tau_{adap}}{\tau_{Ca}}. \tag{17}$$

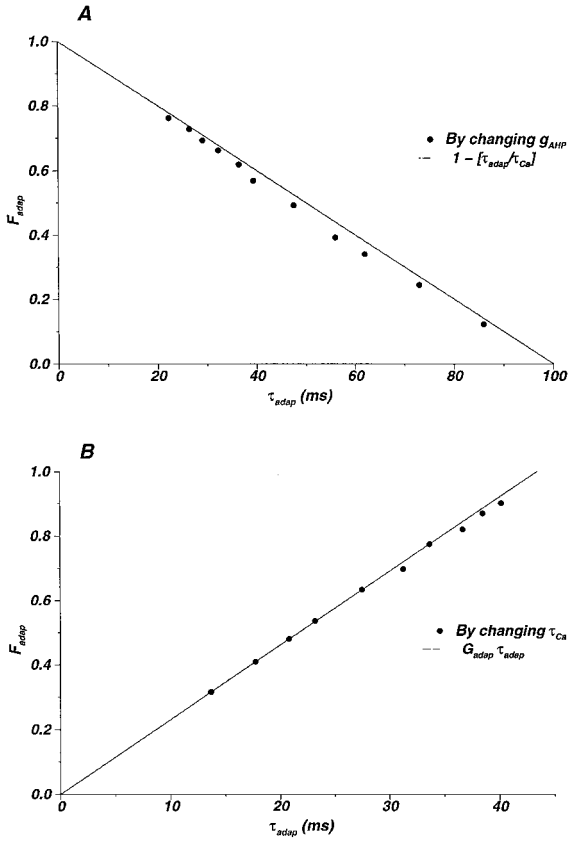

Figure 2. Linear relations between F_{adap} and τ_{Ca}. **A:** A negative linear relation $F_{adap} = 1 - (\tau_{adap}/\tau_{Ca})$ when g_{AHP} is varied. **B:** A positive linear relation $F_{adap} = G_{adap}\tau_{adap}$ when τ_{Ca} is varied. Solid lines: theoretical predictions; filled circles: simulation data. ($\tau_{Ca} =$ 100 ms.)

This theoretical prediction was checked by simulations. We found that the simulation results fit well with the theory. As g_{AHP} is varied from zero to a large value, τ_{adap} and F_{adap} change from $\tau_{adap} = \tau_{Ca}$ and $F_{adap} = 0$ (slow and weak adaptation) to $\tau_{adap} = 0$ and $F_{adap} = 1$ (fast and strong adaptation), along a linear curve (Fig. 2A).

Second, we study the effect of different Ca^{2+} kinetics with a fixed strength of the adaptation conductance. With a slow Ca^{2+} kinetics (large τ_{Ca}), we expect a slow (large τ_{adap}) but strong adaptation (large F_{adap}), since the steady state $[Ca^{2+}]$ is high with slow Ca^{2+} decay, thus inducing a large I_{AHP}. Conversely, a fast Ca^{2+} decay (small τ_{Ca}) induces fast ($\tau_{adap} \to 0$) and ineffective ($F_{adap} \to 0$) adaptation since there is little Ca^{2+} accumulation. Therefore, in this case F_{adap} and τ_{adap} are predicted to vary in the same manner. By substituting $1/\tau_{Ca} = 1/\tau_{adap} - G_{adap}$ (Eq. (15)) into Eq. (17), we have an positive linear relation between F_{adap} and τ_{adap}:

$$F_{adap} = G_{adap}\tau_{adap}. \tag{18}$$

The slope of the linear function is controlled by the factor G_{adap}, which is proportional to αg_{AHP}. The system ranges from a fast and weak adaptation ($\tau_{adap} = 0$ and $F_{adap} = 0$) to a slow and strong adaptation ($\tau_{adap} = 1/G_{adap} \simeq 50$ ms and $F_{adap} = 1$). Note that as τ_{Ca} is varied from zero to ∞, τ_{adap} is varied from zero to $1/G_{adap}$ (here $G_{adap} = 0.023$). Again, the theoretically predicted relation fits well with simulation data (Fig. 2B).

3.3. Dependence of τ_{adap} on Input Drive

The analytical expression for τ_{adap} (Eq. (15)) does not depend on the input current I. On the other hand, experimental data (Ahmed et al., 1998, Fig. 5) and simulations of a conductance-based model (Wang, 1998) showed that τ_{adap} is a weakly increasing function of I. This discrepancy can be reconciled if Eq. (11) is understood as valid for the range of large I values where the f-I curve is approximately linear. At small I values and low firing rates, we have to use the nonlinear f-I relation (Eq. (32)). As shown in Appendix A, in this case we can still derive τ_{adap} based on the fact that $[Ca^{2+}]$ is small in this regime. We found the same expression as Eq. (15), except that $G_{adap}(I)$ now depends on I and is proportional to the slope of the unadapted f-I curve. For injected current inputs, this f-I curve's slope decreases with I (Eq. 32); so does G_{adap}. Consequently, τ_{adap} increases with I, and at large I it converges to a plateau level given by Eq. (15) (Fig. 3A). However, for the I&F model the range of I values over which τ_{adap} varies considerably is quite small (Fig. 3A), unlike conductance-based models (Wang, 1998). Since τ_{adap} depends on the slope of the f-I function (Appendix A), the steeper τ_{adap} curve for the I&F model is probably related to a steeper slope of the f-I function for the I&F model than for the conductance-based model, at low firing rates. For example, if the input is a constant injected current with a firing threshold I_c, the slope of the f-I curve behaves like $\sim 1/((I-I_c)(\ln(1-I_c/I))^2)$ for the I&F model and like $\sim 1/\sqrt{(I-I_c)}$ for the conductance-based model considered in Wang (1998) (see also Ermentrout, 1998).

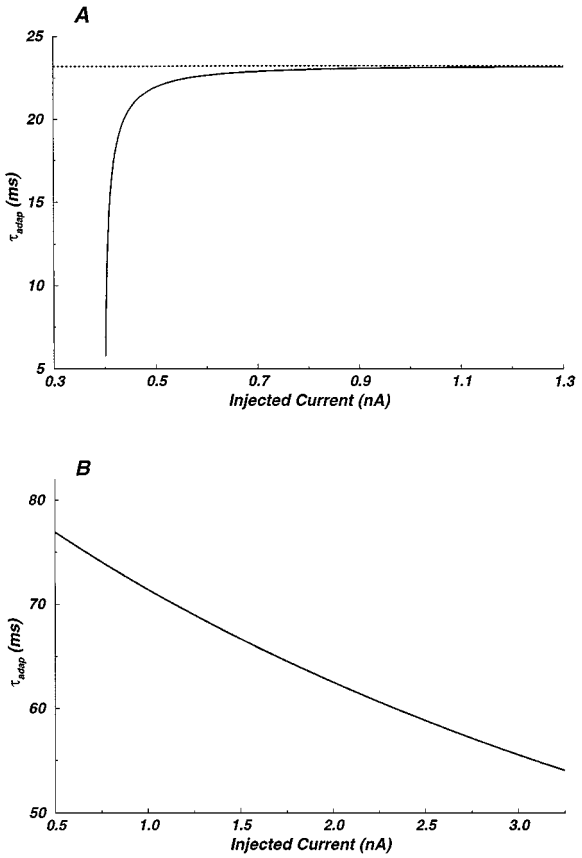

Figure 3. τ_{adap} is dependent on the amplitude of the input drive. **A:** For the I_{AHP} model, τ_{adap} is an increasing function of the amplitude of the input drive (Eq. (41)); it approaches the input-independent value determined by Eq. (15) asymptotically with large input drive. **B:** For the threshold adaptation model, τ_{adap} decreases strongly with the input drive over a wide range (Eq. (19)).

3.4. *Adaptation Time Course for the Threshold Model*

We also simulated and analytically studied the scenario where spike-frequency adaptation is produced by a dynamical voltage threshold. In this case, the firing rate f depends on the threshold θ in a nonlinear manner, and the nonlinear averaged equation for the slow variable $\theta(t)$ does not yield a mono-exponential time evolution. In addition, we found that the threshold model usually does not display sufficiently strong adaptation comparable with the data from cortical pyramidal neurons, unless the change in voltage threshold is large. For instance, in Fig. 4B the instantaneous firing rate is decreased from $f_{init} \simeq 200$ Hz to $f_{ss} \simeq 50\,Hz$, as the threshold θ is increased from 3 mV to 15 mV. On the other hand, if the adaptation is weak (Fig. 4A), the total increase in θ is small compared with θ_0. Then $f(\theta)$ can be linearized, the adaptation time course can be approximated with a mono-exponential, and an adaptation time constant can be explicitly derived. In particular, with the synaptic inputs converted into an equivalent current I_{eff}, τ_{adap} is given by

$$\tau_{adap} = \left[\frac{1}{\tau_\theta} + \frac{\alpha' I_{eff}}{C_m \theta_0^2}\right]^{-1} \tag{19}$$

with $I_{eff} = I - g(V_{reset} - V_{rest})$. Note that, in contrast to the I_{AHP} model, the adaptation time constant strongly depends on the input amplitude and *decreases* with larger input drive over a broad range (Fig. 3B).

The adaptation time courses of θ and f are given by

$$\theta(t) = \theta_0 + \Delta\theta_{ss}(1 - e^{-t/\tau_{adap}}) \tag{20}$$

$$f(t) = f_{ss} + (f_{init} - f_{ss})e^{-t/\tau_{adap}}, \tag{21}$$

with $f_{init} = 350$ Hz, $f_{ss} = 265$ Hz, and $\tau_{adap} = 60.6$ ms. The theoretically derived time courses for $f(t)$ and $\theta(t)$ are superimposed on the simulation data in Fig. 4A. The degree of adaptation has a similar relationship with τ_{adap} as in the I_{AHP} model

$$F_{adap} \equiv \frac{f_{init} - f_{ss}}{f_{init}} = 1 - \frac{\tau_{adap}}{\tau_\theta}. \tag{22}$$

For the threshold model, as the firing rate decreases in time, the ISI $CV(t)$ may either decrease (Fig. 4A, bottom panel), increase (not shown), or first decrease rapidly and then increase slowly to a steady-state value (Fig. 4B, bottom panel). This is in contrast with the I_{AHP} model, for which CV always increases monotonically in time (cf. Fig. 1D). This difference between these two adaptation models will be further examined in the next section.

3.5. *Time Course of the ISI Variability: Comparison Between the Two Models*

For either the I_{AHP} model or threshold model, the spike-frequency adaptation time course may be viewed in terms of a *standard* integrate-and-fire neuron with a parameter ($[Ca^{2+}]$ or θ, respectively) increasing slowly from an initial value to a steady-state value. Therefore, in order to understand the time evolution of the CV during the adaptation process, we considered how the CV of a standard integrate-and-fire model depends on

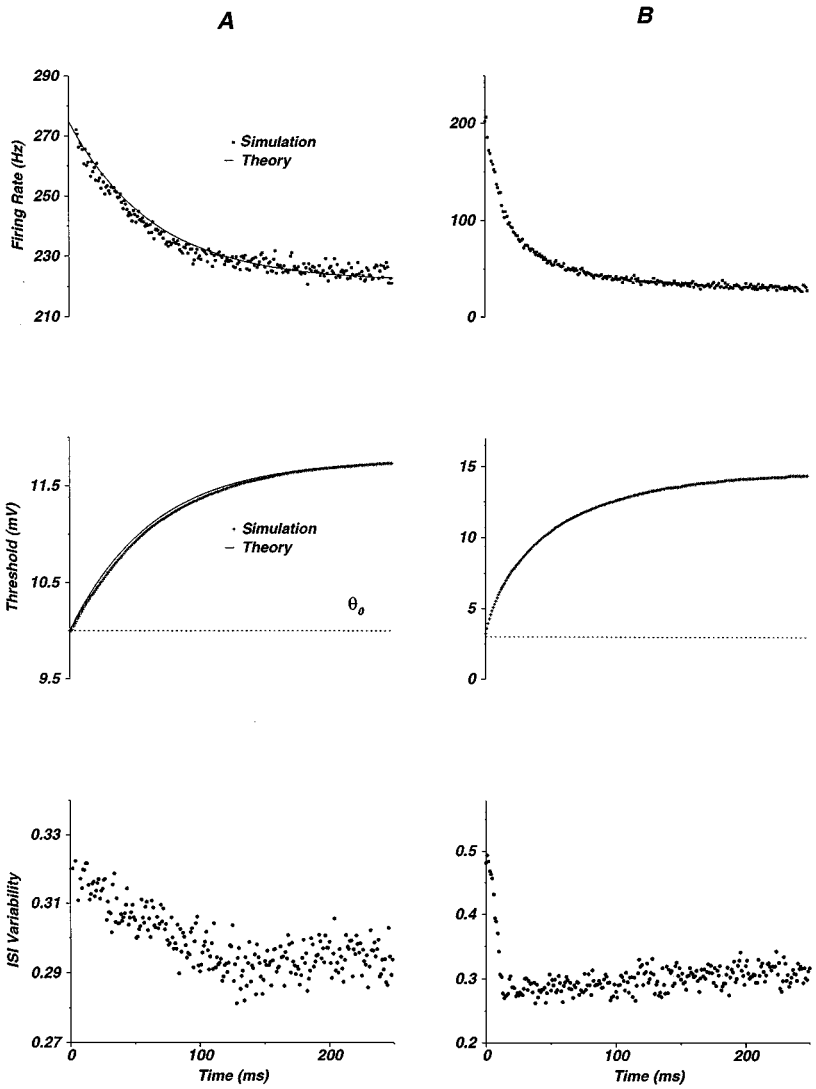

Figure 4. Simulation results of adaptation process for threshold model. **A:** When $\Delta\theta \ll \theta_0$, there exists an adaptation time constant that is dependent on the amplitude of the input drive. Threshold approaches θ_{ss} with the same adaptation time constant. The *ISI* variability always decreases during the adaptation process when the input drive is strong enough. ($\theta_0 = 10$ mV, $\alpha = 0.1$ mV.) **B:** When θ goes through a very broad range, the adaptation time course can no longer be fitted with a single time constant. *ISI* variability shows complicated changes; it first decreases rapidly and then increases slowly to steady-state value. ($\theta_0 = 3$ mV, $\alpha = 2$ mV.)

the value of the slowly varying parameter ($[Ca^{2+}]$ or θ). The *CV* of a Poisson input spike train is 1. For the integrate-and-fire model driven by Poisson inputs, due to the integration effect, the *CV* of the output ISIs is always less than 1. With a given threshold θ, the variability of ISIs decreases smoothly from 1 to $\sqrt{\Delta V/\theta}$ as the firing rate increases from zero to infinity (Softky and Koch, 1993) as shown in Fig. 5A. This is because the higher the firing rate, the less passive decay for the membrane voltage. Thus, with a high firing rate the neuron functions like an integrator with smaller output variability. With a low firing rate, V_m decays back to about V_{rest} between synaptic inputs, and spikes are triggered more likely by temporally coincident inputs than by integration of inputs over time. Thus the neuron functions as a coincidence detector with a larger output variability.

For the I_{AHP} model, we observed that during the adaptation process *CV* increased in time with a time course similar to that of the decrease in the firing rate

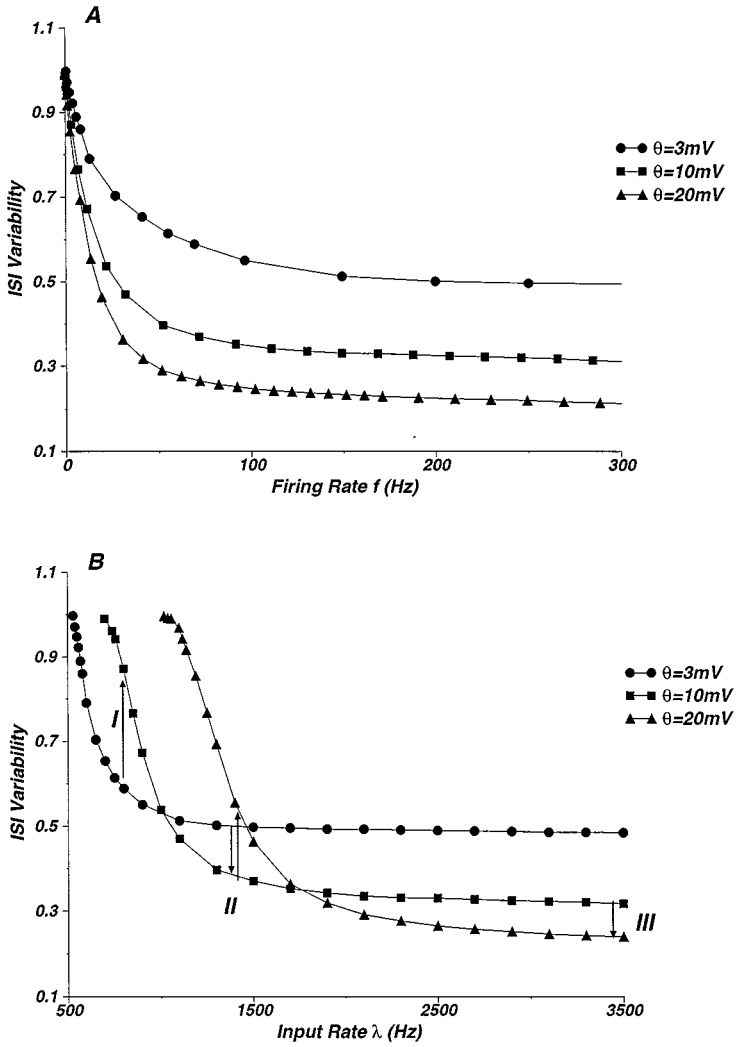

Figure 5. Variability of the *ISI*s of the I&F model. **A:** For different thresholds, *CV* decreases smoothly from 1 to $\sqrt{\Delta V/\theta}$ as the mean firing rate increases from zero to infinity. **B:** When *CV* is plotted versus input rate λ, the curves for different thresholds intersect with each other. Thus an increase in the threshold may lead to different time courses of *CV*. Type (*I*), when the input drive is weak, *ISI* variability increases. Type (*II*), *ISI* variability first decreases and then increases. Type (*III*), with a large enough drive *ISI* variability always decreases monotonically.

(Fig. 1D). This can be explained by considering Fig. 5A for the integrate-and-fire model: *CV* is a monotonically decreasing function of the firing rate.

By contrast, for the threshold model, *CV* may decrease or evolve nonmonotonically in time as the firing rate f is reduced by adaptation (Fig. 4). This finding can be explained as the following. Two *CV*-versus-f curves with different θ values do not cross with each other (Fig. 5A). That is, with a fixed firing rate, the neuron with a smaller threshold displays a larger ISI variability (because less integration of inputs is needed to reach the firing threshold). However, if plotted against the input rate λ rather than f, the *CV* curves with different θ values intersect with each other (Fig. 5B). Consider, for instance, two curves with $\theta_1 = 10$ mV and $\theta_2 = 3$ mV (filled square and circle in Fig. 5B). The θ_1 curve starts at a larger λ value than the θ_2 curve because with a larger threshold a stronger input drive is required to trigger repetitive discharges. At the onset of the θ_1 curve, the firing is Poisson-like with a $CV \simeq 1$, larger than the *CV* for θ_2 at the same λ. On the other hand, at sufficiently large λ values, we know that the neuron must fire more regularly with a larger θ; thus *CV* is smaller with θ_1 than with θ_2 ($CV \to \sqrt{\Delta V/\theta}$).

Therefore, the two curves for θ_1 and θ_2 must intersect at least once. As θ increases during adaptation, the time course of $CV(t)$ is equivalent to moving along the vertical line labeling the same input rate, from a curve (corresponding to the initial θ_0) to another curve (corresponding to the increased θ_{ss}) (Fig. 5B). As a consequence, *CV* may either increase or decrease during the adaptation process, depending on the θ_0 and θ_{ss} values and the input rate λ. If λ is smaller than the intersection point of the two curves, *CV* increases monotonically during the adaptation process. But with a sufficiently large input rates ($\lambda = 3500$ Hz as in Fig. 4A), *CV* monotonically *decreases*. The nonmonotonic time course shown in Fig. 4B can be interpreted by considering Fig. 5B with $\lambda = 1500$ Hz (used in Fig. 4B). Along this vertical line, as θ increases from 3 mV toward 20 mV, *CV* first decreases and then increases in time, thus exhibiting a nonmonotonic behavior.

3.6. Temporal Statistics of Spike Trains in Stationary State

The trial-averaged firing rate eventually reaches a steady-state level after the transient adaptation process. However, even in this stationary state, in each trial the Poisson input varies randomly in time; therefore, the neural firing pattern is still modulated by the dynamics of I_{AHP}. We shall now discuss the effects of the I_{AHP} on the temporal structure of spike trains in the stationary-state situation. For comparison, let us first consider the case when there is no adaptation ($g_{AHP} = 0$). A sample spike train is shown in Fig. 6A (upper panel); its statistical properties are characterized by an ISI histogram and an ISI return map. The ISI histogram is simple (can be approximated by a Gamma function) as shown in Fig. 6A (middle panel), with an average ISI = 16 ms and $CV = 0.61$. The ISI return map, where each ISI_{i+1} is plotted versus its preceding value ISI_i, describes the

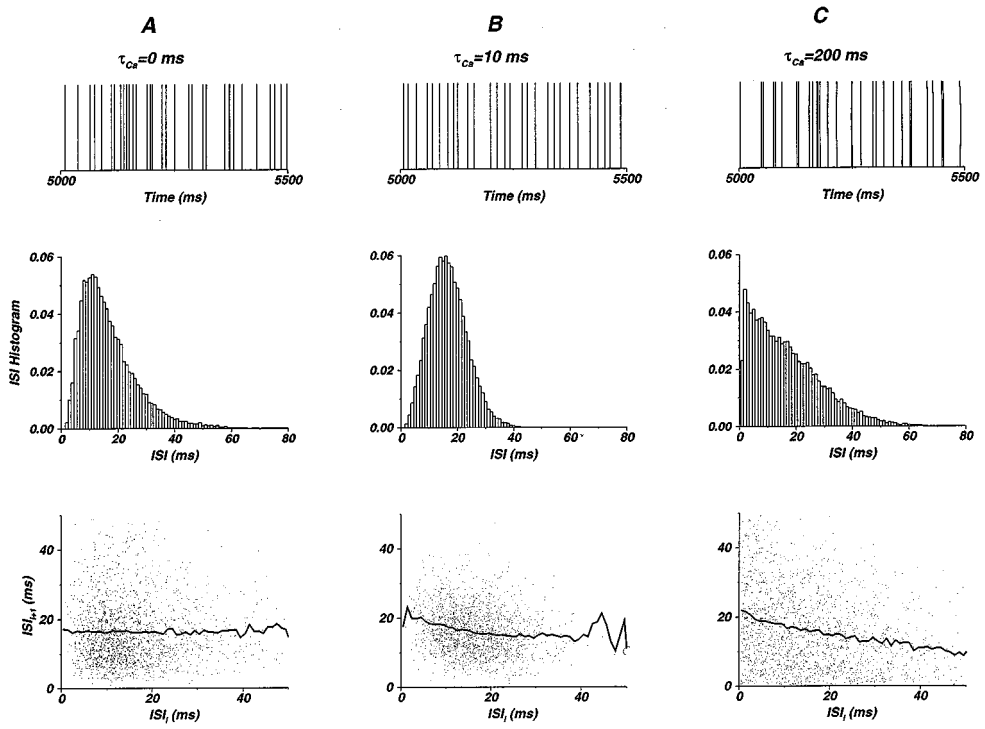

Figure 6. Adaptation can alter the temporal structure of the output spike train. All spike trains have the same mean *ISI* $\sim$ 16 ms. Upper panel: a typical spike train; middle panel: the *ISI* histogram; lower panel: the *ISI* return map and the conditional mean of ISI_{i+1} for ISI_i (solid curve). **A:** When there is no adaptation, there is no correlation between consecutive *ISI*s as indicated by the flat conditional average curve. **B:** With $g_{AHP} = 0.02$ and $\tau_{Ca} = 10$ ms, the *ISI* histogram is narrower with a smaller *CV*. There is negative correlation between consecutive *ISI*s. **C:** With $g_{AHP} = 0.02$ and $\tau_{Ca} = 200$ ms, the *ISI* histogram is broader with a larger *CV*. The negative correlation between consecutive *ISI*s is even more pronounced.

temporal relations between consecutive ISIs (Fig. 6A, lower panel). The solid curve is the conditional average of ISI_{i+1}, calculated for each ISI_i value. The fact that it is a flat function of ISI_i ($CC \simeq 0$) means that the expected value of ISI_{i+1} is independent of ISI_i—that is, there is little correlation between consecutive ISIs when the input is Poisson and temporally uncorrelated.

By contrast, with firing-rate adaptation ($g_{AHP} \neq 0$), the spike firing patterns are modulated by the dynamics of the I_{AHP} in an interesting manner (Fig. 6). In all three cases of Fig. 6, the steady-state mean ISI ($\sim$16 ms) was maintained to be the same by adjusting input rate λ values. We found that *CV* can be either reduced or increased by the Ca^{2+}-mediated I_{AHP}, depending on the $[Ca^{2+}]$ decay-time constant τ_{Ca}. If τ_{Ca} is short compared with the mean ISI of the spike train, the spike train is modulated to be *less* variable during steady state. An example with $\tau_{Ca} = 10$ ms is shown in Fig. 6B, with a much more regular spike train (upper panel) and a narrower ISI histogram (smaller $CV = 0.41$, middle panel) than in Fig. 6A. On the other hand, if τ_{Ca} is much larger than the mean ISI of the spike train, the neuronal discharges in steady state are more random and Poisson-like, as illustrated by the example in Fig. 6C with $\tau_{Ca} = 200$ ms, where the spike train is quite irregular and the ISIH becomes almost exponential (Poisson-like) with larger $CV = 0.74$.

Furthermore, significant temporal correlations in the spike train are created by the Ca^{2+}-mediated I_{AHP}. As shown by the ISI return maps (Fig. 6B–C, lower panels), the curves of conditional ISI average show a negative slope, $CC = -0.18$ in (B) and -0.24 in (C). These imply that the smaller is an ISI_i, the larger is the next ISI_{i+1} expected to be, and vice versa. This anticorrelation can be understood as follows: if by chance the firing rate is high (small ISI_i) at some time, the outward I_{AHP} current is accumulated significantly, reducing the cell's excitability; therefore, a low firing rate (large ISI_{i+1}) is expected subsequently.

Thus the adapting current I_{AHP} not only changes the mean rate of the spike train but also alters the temporal structure in the spike train even in steady state.

3.7. *The Dependence of CV and CC on τ_{Ca}*

We found that both *CV* and *CC* of the steady-state spike train are nonmonotonic functions of the $[Ca^{2+}]$ decay-time constant τ_{Ca} (Fig. 7). Consistent with the findings of Fig. 6, the *CV* is reduced (respectively, increased) if τ_{Ca} is small (respectively, large) compared with the mean ISI (Fig. 7A, left panel). (The control case without adaptation corresponds to $\tau_{Ca} = 0$.) These observations can be understood as follows. With a large τ_{Ca}, in the steady state the mean $[Ca^{2+}]$ reaches a steady-state level $[Ca^{2+}]_{ss}$, and the mean plateau $g_{AHP}[Ca^{2+}]_{ss}$ acts as a "leak" conductance. The increase in the *CV* can then be explained by a significant reduction of the effective membrane time constant $1/\tau_m^\star = 1/\tau_m + g_{AHP}[Ca^{2+}]_{ss}/C_m$ (cf. Eq. (30), Appendix A). For example, in Fig. 1, $[Ca^{2+}]_{ss} = 1.43\,\mu$M, $\tau_m^\star = 11$ ms while $\tau_m = 20$ ms; thus the time constant is reduced almost by 100%. Thus the cell functions more like a coincidence detector, and the output spike train has a larger *CV*. On the other hand, with a small τ_{Ca}, $[Ca^{2+}]$ decays greatly between spikes and g_{AHP} cannot accumulate in time, and there is negligible net decrease in the input resistance. Instead, the rapid adaptation dynamics suppresses clustering of spikes (which is associated with the ISI variability when $g_{AHP} = 0$), so that the spikes become more evenly distributed in time (Fig. 6B) and *CV* is smaller than without adaptation.

Therefore, there is a critical value of τ_{Ca}, above which the steady-state *CV* is larger with the adapting I_{AHP} than without it. This critical τ_{Ca} was found to be insensitive to the adaptation strength (g_{AHP}), though a larger g_{AHP} yields a greater change in the *CV* (data not shown). On the other hand, this critical τ_{Ca} depends strongly on the mean ISI ($< \Delta t >$) of the spike train. For instance, it is about 75 ms with $< \Delta t > = 16$ ms, and greater than 400 ms for $< \Delta t > = 45$ ms (Fig. 7A). In Fig. 1, where the steady state $< \Delta t >$ is small ($\sim$7 ms), the critical τ_{Ca} is small, and as a result $\tau_{Ca} = 50$ ms in the simulation yields a spike train with larger *CV* than in the case without adaptation, at the same firing rate.

The dependence of *CC* on τ_{Ca} is also complicated. With the same mean firing rate, *CC* is negative for all τ_{Ca} values (Fig. 7B). However, the *CC* curve exhibits a negative peak at a τ_{Ca} value comparable with the mean ISI $< \Delta t >$. This is because, if τ_{Ca} is too short compared with $< \Delta t >$, $[Ca^{2+}]$ cannot accumulate, and the anticorrelation effect is small. If τ_{Ca} is very long, the temporal $[Ca^{2+}]$ fluctuations are small compared with its steady-state average—that is, the change of $[Ca^{2+}]$ over two consecutive ISIs is small, and hence the anticorrelation is again weak. The same phenomenon is illustrated in a different way in Fig. 8A. Here, τ_{Ca} is fixed, but the mean ISI $< \Delta t >$ is varied by changing λ. *CC* as function of the output rate displays a strong

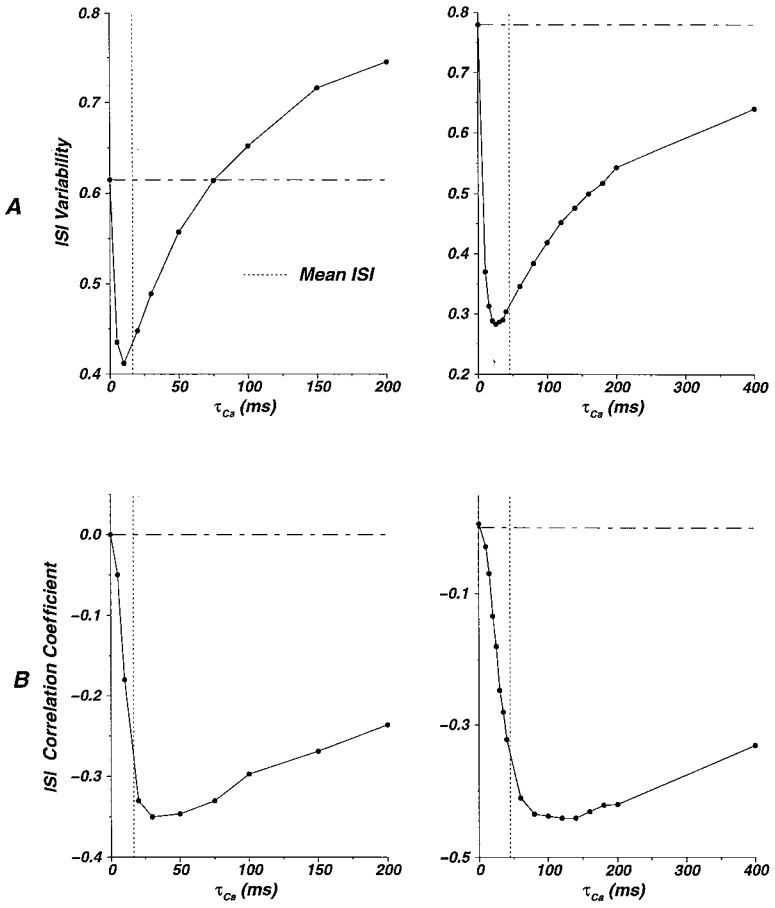

Figure 7. *CV* and *CC* strongly depend on τ_{Ca} The input rate λ is adjusted to maintain the same output firing rate (the mean *ISI* is denoted by the vertical dotted lines, 16 ms for left graphs and 45 ms for the right graphs). **A:** *CV* first decreases and then increases with increasing τ_{Ca}. *CV* without adaptation is indicated by the horizontal dashed line. **B:** *CC* first decreases and then increases with increasing τ_{Ca}. *CC* without adaptation is indicated by the horizontal dashed line. ($g_{AHP} = 0.02$.).

negative peak at about 20 Hz. Again, *CC* is negligible at very low rates when $< \Delta t >$ is large compared with τ_{Ca}, and *CC* is also small at high rates when temporal fluctuations of $[Ca^{2+}]$ are negligible compared with its average.

As expected, for a fixed τ_{Ca}, a larger g_{AHP} yields stronger negative correlations between consecutive ISIs in the steady state (Fig. 8B). Thus the correlation coefficient *CC* can be used as a measure of the strength of neuronal adaptation mechanism provided that the input is uncorrelated in time.

3.8. Forward Masking

As we argued earlier, spike-frequency adaptation is a cellular form of delayed inhibition of the neuron on itself. As such, it may subserve a mechanism for temporal (inhibitory) interaction between responses to input signals from different sources. In the cricket auditory system, when stimulated by sound inputs from both ears, the omega cells were shown to selectively respond to the stronger input, whereas its normal response to the weaker input (observed when the latter was presented alone) was suppressed (Pollack, 1988). *In vivo* calcium imaging and intracellular recording data suggest that this effect is produced by a Ca^{2+}-activated hyperpolarizing current (Sobel and Tank, 1994). We found that our model displayed a similar phenomenon, suggesting that this forward masking effect is expected in general for all strongly adapting neurons.

For an integrate-and-fire neuron, there is little interference between the cell's responses to two different inputs, and the neuronal discharges are additive.

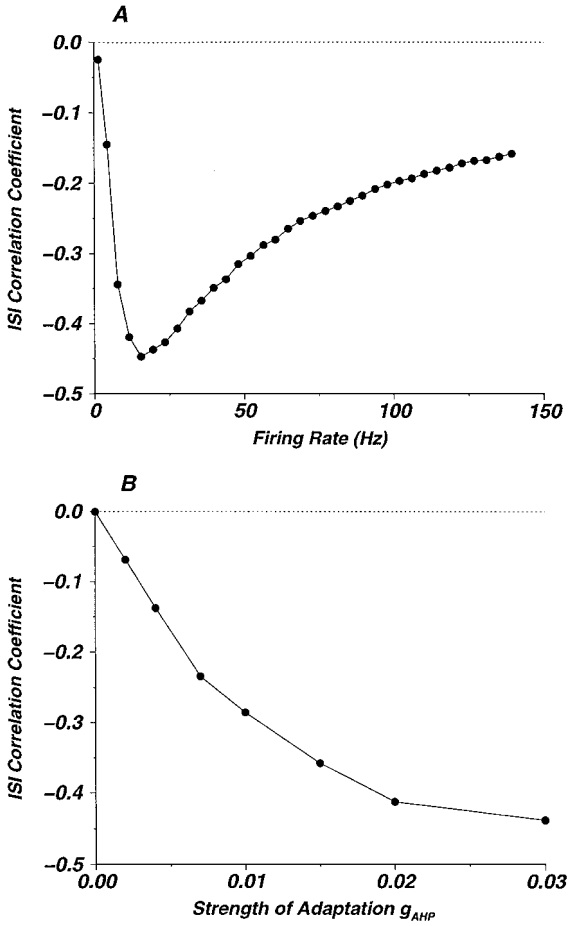

Figure 8. *CC* is affected by mean firing rate and adaptation strength g_{AHP}. **A:** With fixed τ_{Ca} and g_{AHP}, *CC* is a function of mean firing rate (by changing the input rate λ), with a minimum at mean rate around 20 Hz ($\sim 1/\tau_{Ca}$, $\tau_{Ca} = 50$ ms). **B:** With fixed input rate λ and τ_{Ca}, larger adaptation strength g_{AHP} induces stronger negative correlation (negative *CC*) between consecutive *ISI*s.

This is no longer the case in the presence of the adapting current I_{AHP}. For example, in response to a periodic train (at 2.5 Hz) of square input pulses (width 100 ms) with Poisson rate $\lambda_1 = 2000$ Hz, the model neuron fires at 20 to 40 Hz (2 to 4 spikes per input pulse of 100 ms) (Fig. 9A). However, if there is a second train of square pulses with a larger amplitude (Poisson rate $\lambda_2 = 4000$ Hz), phase-shifted from the first input train, the neuron's response to the weaker input is quickly suppressed after a few cycles (Fig. 9B). We distinguish here two related but different effects. On the one hand, there is a *phasic* forward masking effect (Sobel and Tank, 1994): if stronger input pulses occur just before the weaker ones (Fig. 9C), the firing response to the stronger input triggers a significant Ca^{2+} influx (Fig. 9C, upper panel), the increased I_{AHP} reduces the cell's excitability, and hence the response to the weaker input is suppressed (Fig. 9C, middle panel). Here, the condition is that the time interval between the stronger and weaker inputs should be short compared with τ_{Ca}. On the other hand, there is a *tonic* effect: if the *period* of the repetitive input trains is not too long compared with τ_{Ca}, there is a significant $[Ca^{2+}]$ plateau in time, and the resulting *mean* I_{AHP} reduces the cell's responses to both weaker and stronger inputs. However, we found that the response to the weaker signal is much more strongly suppressed than that to the stronger signal. The effect is not sensitive to the relative temporal relations of the two signals, and there is still a selective suppression even when input pulses from the weaker signal occur just before those from the stronger signal (Fig. 9D). This second effect is different from the simple forward masking effect and is predominant when τ_{Ca} is sufficiently large compared with the period of the input pulses.

Can the forward masking mechanism take place quickly after the competing signals are introduced? In Fig. 10A, we plotted the response ratio (R_2/R_1) (R_i being the number of spikes per pulse, invoked by signal i, $i = 1, 2$) as a function of the number of input pulse pairs in time. We found that the onset is rapid, and (R_2/R_1) reaches the plateau after 4 to 5 input pulse pairs. This is true independent of whether the very first input pulse is from the weaker or stronger stimulus. The key for the rapid onset is that $[Ca^{2+}]$ (hence I_{AHP}) builds up quickly during stimulations with a small time constant τ_{adap} and yet decays slowly between stimulations with a large time constant τ_{Ca}, so that a significant level of I_{AHP} is reached quickly to effectively suppresses the response to the weak input signal. As expected, the forward masking effect is stronger with larger g_{AHP} and τ_{Ca} values (Fig. 10B).

Why is the suppression selective to the weaker input? The I_{AHP} reduces the cell's response to *both* weaker and stronger inputs: the response to each input is smaller than it would be in the absence of the other input. Again there are two factors, one due to phasic transients and the other due to the tonic $[Ca^{2+}]$ plateau. As illustrated by the example in Fig. 9, because the stronger response generates a much larger Ca^{2+} influx, I_{AHP} is high at the onset of the following weaker pulse. Therefore, the weaker response is small, which in turns allows $[Ca^{2+}]$ (hence I_{AHP}) to decay further

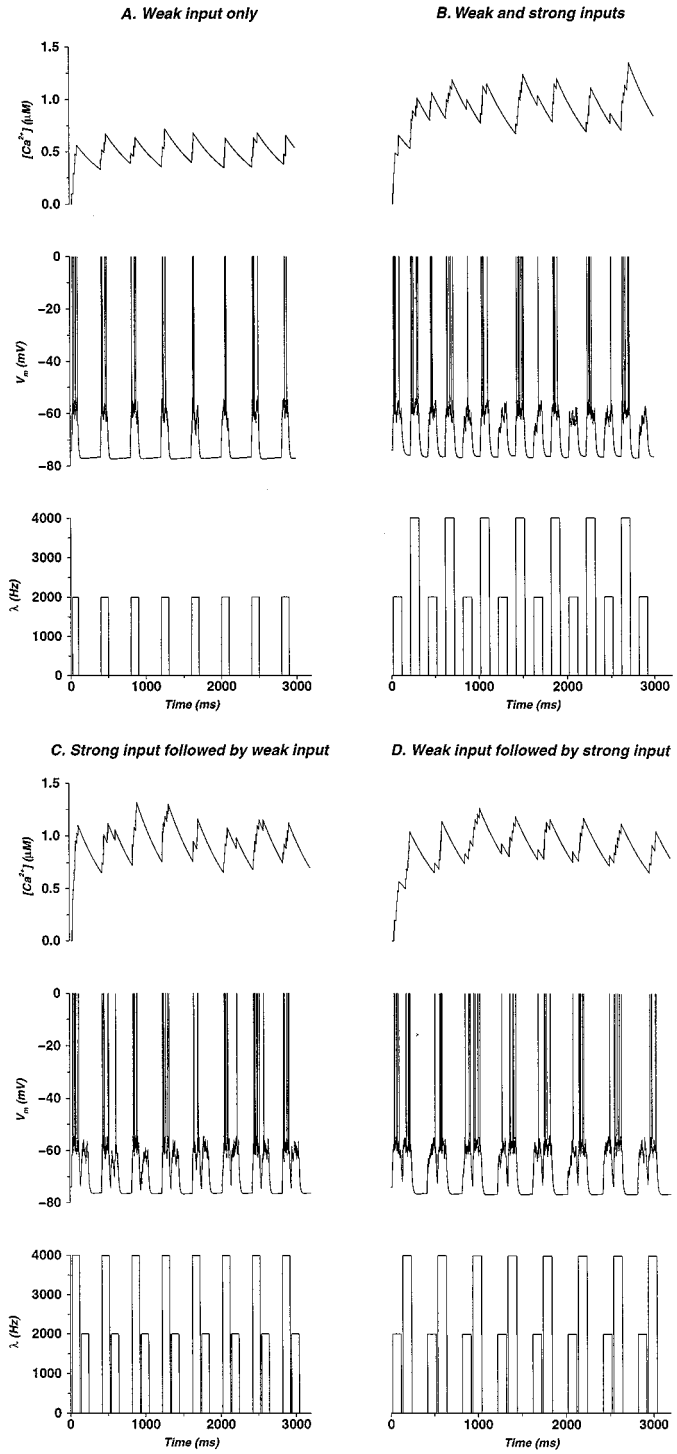

Figure 9. Forward masking is induced by adaptation when there are two competing input sources. The response to the stronger input suppresses that to the weaker one. **A:** The $[Ca^{2+}]$ dynamics, the membrane voltage and the input rate are shown. The input consists of weak input source only. **B:** The input consists alternatively of weak and strong inputs. The response to the weak input is strongly suppressed due to the presence of the strong input. **C–D:** The suppression is not sensitive to the relative temporal phase of inputs from the two sources. ($g_{AHP} = 0.05$, $\alpha = 0.1$, $\tau_{Ca} = 600$ ms.).

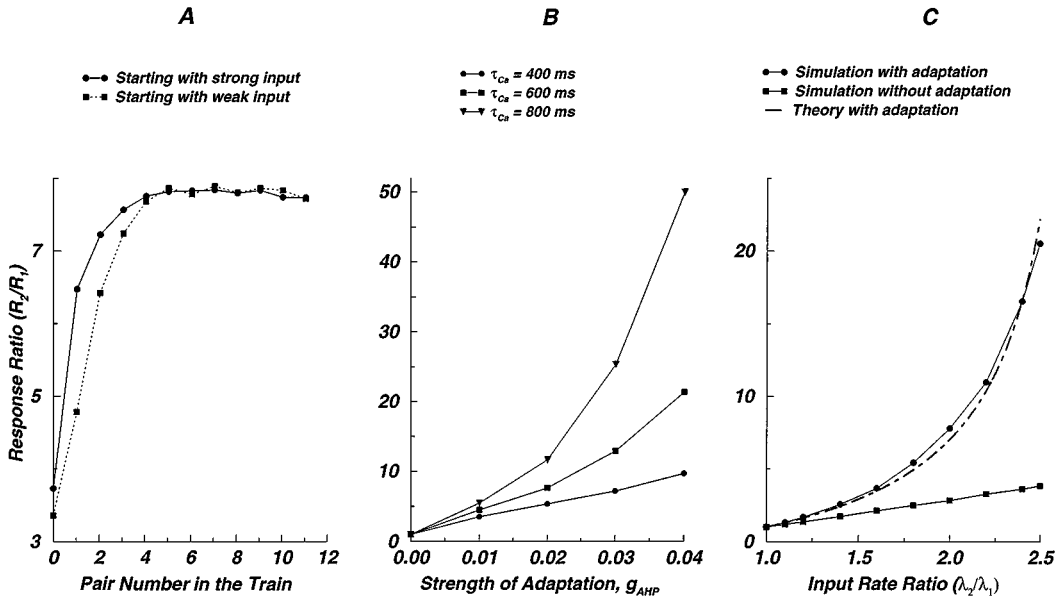

Figure 10. Quantitative examination of the forward masking effect. **A:** For each pair of the strong and weak input pulses in a train, the response ratio is plotted as a function of the pulse pair sequence number since the onset. The induction of suppression is fast, reaching the saturation in a few pairs (1−2 sec). The order of weak and strong input pulses within a pair is not important for the induction of suppression. **B:** The response ratio also depends on the calcium decay time constant τ_{Ca} and strength of adaptation g_{AHP}. Larger τ_{Ca} or g_{AHP} enhances the forward masking effect. **C:** Without adaptation, the responses ratio for the strong and weak inputs are linear with the input rate ratio. With adaptation-induced forward masking, the responses ratio for the strong and weak inputs becomes a highly nonlinear function of the input rate ratio. The thereotically predicted nonlinear curve for response ratio fits well with simulation results.

until the next stronger input arrives. Consequently, I_{AHP} is significantly smaller at the arrival time of a stronger input pulse than that of a weaker one, this *temporal pattern* of $[Ca^{2+}]$ and I_{AHP} contribute to the suppression selectivity. One the other hand, we show in Appendix B that for large τ_{Ca}, even when $[Ca^{2+}]$ does not fluctuate significantly in time, there is still a selectivity simply because the response ratio is a nonlinear function of the input ratio. In Fig. 10C, this selectivity is quantified by plotted the time-averaged output ratio (R_2/R_1) versus the input ratio (λ_2/λ_1). As a control, the response ratio is first computed in the absence of I_{AHP}. If there is no adaptation, (R_2/R_1) is almost linear with (λ_2/λ_1). This is easy to understand if we consider the linearity between the input strength and firing rate. By contrast, with adaptation, the response ratio is a highly nonlinear function of the input ratio (Fig. 10C), which can be theoretically derived (Appendix B):

$$\frac{R_2}{R_1} = \frac{f_2}{f_1} = \frac{\rho(I_2/I_1) - 1}{\rho - (I_2/I_1)}, \qquad (23)$$

where $I_2/I_1 < \rho$, $I_i = \lambda_i \Delta V C_m - g(V_{reset} - V_{rest}) - C_m\theta/(2\tau_m)$, $i = 1, 2$. ρ is a constant independent of I_1 and I_2. In our simulation, $\rho \sim 4.3$. The analytical prediction (dott-dashed curve) agrees well with numerical simulations (solid curve).

If $I_2/I_1 \geq \rho$, the response to the weak pulse is totally masked. In our simulation, this corresponds to the input ratio $(\lambda_2/\lambda_1) \geq 2.6$. This means that when the synaptic input drive of the stronger signal is more than 2.6 times of that of the weaker signal, the neuron does not have any response to the weaker signal. The nonlinear forward-masking effect induced by the slow I_{AHP} current can be understood as the following: when the fluctuation of I_{AHP} is small compared with its steady-state level, it gives rise to a tonic hyperpolarizing current that is a function of both I_1 and I_2. As the response ratio is roughly I_2/I_1 without adaptation, with the inhibitory current the response ratio is $(I_2 - I_{AHP})/(I_1 - I_{AHP})$, which is a nonlinear function of the input ratio I_2/I_1. Moreover, I_{AHP} itsef is also a function of the input ration I_2/I_1. These two factors lead to the nonlinear forward masking effect, even though the system is approximately linear.

4. Discussion

4.1. Spike-Frequency Adaptation of a Generalized I&F Model

In this work, we studied a generalized integrate-and-fire neuron model that takes into account spike-frequency adaptation (see also Treves, 1993; Stemmler et al., 1995; Troyer and Miller, 1997). The inclusion of a Ca^{2+}-activated K^+ current I_{AHP} involves three additional parameters: the Ca^{2+} influx per action potential α, the $[Ca^{2+}]$ decay time constant τ_{Ca}, and the ionic conductance g_{AHP}. For a given cell type such as cortical pyramidal neurons, α and τ_{Ca} can be measured by Ca^{2+} imaging techniques (Schiller et al., 1995; Helmchen et al., 1996; Svoboda et al., 1997). On the other hand, g_{AHP} can be derived from voltage-clamp experiments on the I_{AHP}. Hence, in principle all these parameters can be fitted by experimental data.

We were particularly motivated by the recent experimental finding of Ahmed et al. (1998) that, in the cat visual cortical neurons, the spike-frequency adaptation to a current pulse stimulation can be well fitted by a single exponential time course, characterized by a time constant τ_{adap} and the degree of adaptation F_{adap}. With our model, we could predict this time course of adaptation analytically at sufficiently high firing rates and express τ_{adap} and F_{adap} in terms of the membrane and calcium parameters. At low firing rates, simple analytical predictions are not feasible because the f-I curve is nonlinear, and it is not given by a compact expression for noisy Poisson inputs (Ricciardi, 1977).

We also considered an alternative model, where the adaptation is due to an incremental increase in the voltage firing threshold θ. Although both models behave similarly in some ways, they differ in at least three aspects. First, in order to obtain strong adaptation (such as $F_{adap} > 50\%$), in the threshold model θ would have to change by as much as 10 mV (Fig. 4B), which is not the case for the I_{AHP} model. Second, τ_{adap} increases with input amplitude in the I_{AHP} model, whereas the opposite is predicted by the threshold model (Fig. 3). Third, with a stochastic Poisson input, the instantaneous ISI variability always increases during the adaptation onset for the I_{AHP} model (Fig. 1) but can either decrease or be nonmonotonic in time for the threshold model (Fig. 4). Measurements from cortical pyramidal cells show an increased τ_{adap} as function of the input current intensity (Ahmed et al., 1998), in support of a current subtraction rather than a voltage threshold mechanism for adaptation in cortical pyramidal neurons. Further experiments are worthwhile to test the two alternative models.

4.2. Comparison Between the Model and Cortical Pyramidal Neurons

In our I_{AHP} model, τ_{adap} and F_{adap} are controlled by τ_{Ca} and αg_{AHP} and obey two simple relations: $F_{adap} = 1-\tau_{adap}/\tau_{Ca}$ (Eq. (17)), and $F_{adap} = G_{adap}\tau_{adap}$, where G_{adap} is proportional to αg_{AHP} but independent of τ_{Ca} (Eq. (18)). These two relations are quite useful. For example, simply by measuring F_{adap} and τ_{adap} we can estimate the $[Ca^{2+}]$ decay time constant τ_{Ca} using Eq. (17). It is likely that for real cortical pyramidal neurons, the two relations hold only approximately because many factors not included in our model may quantitatively affect the spike-adaptation properties.

Nevertheless, the success of Ahmed et al. (1998) in fitting the data by single exponentials indicate that our model may have captured the predominant features of spike-frequency adaptation in cortical pyramidal cells, at least at the time-scale of a few hundreds of milliseconds. In order to test our model further, the two relations between τ_{adap} and F_{adap} should be assessed experimentally by plotting data points for F_{adap} and τ_{adap} against each other. For example, the first relation should hold for different F_{adap} and τ_{adap} values obtained by pharmacologically enhancing or blocking the g_{AHP} to various degrees. On the other hand, if the $[Ca^{2+}]$ decay kinetics are changed, the second relation between F_{adap} and τ_{adap} is predicted.

Ahmed et al. (1998) showed that F_{adap} and τ_{adap} correlate significantly with cortical depth. Neurons from superficial layers (layers II to IV) adapt more quickly and to a greater degree ($\tau_{adap} \sim 3 - 24$ ms (mean = 11 ms), and $F_{adap} \sim 55-80\%$ (mean = 67%)) than neurons in deep layers (layers V to VI, $\tau_{adap} \sim 24 - 75$ ms (mean = 50 ms) and $F_{adap} \sim 35 - 65\%$ (mean = 51%)). These observations can be accounted for as follows. By applying $F_{adap} = 1 - \tau_{adap}/\tau_{Ca}$, we predict that in layers II to IV neurons $\tau_{Ca} \simeq 40$ ms, while in deeper layers V to VI neurons $\tau_{Ca} \simeq 100$ ms, thus pyramidal neurons in superficial layers have faster calcium dynamics. On the other hand, by applying $F_{adap} = G_{adap}\tau_{adap}$, we conclude that αg_{AHP} is likely to be much larger (almost 6 times) for neurons in superficial layers than for those in deep layers.

4.3. *Neuronal Adaptation and Temporal Structure of Spike Trains*

With stochastic synaptic inputs to drive the model neuron, we found that the I_{AHP} affects the temporal structure of the output spike train in several interesting ways, even in the stationary state after the adaptation onset. First, when the input is Poisson (without temporal correlation), the Ca^{2+}-activated I_{AHP} dramatically affects the output ISI variability (*CV*). Much work has been devoted to the question of temporal structure and variability in the neuronal output (Calvin and Stevens, 1968; Softky and Koch, 1993; Shadlen and Newsome, 1994; Softky, 1995; Gabbiani and Koch, 1996; Holt et al., 1996; van Vreeswijk and Sompolinsky, 1996; Troyer and Miller, 1997; Rieke et al., 1997). Here, we found that the *CV* can be reduced or enhanced by adaptation, if the time constant of the Ca^{2+}-dependent feedback is small or large compared with the mean ISI, respectively. We speculate that this should hold true for other forms of self-inhibition mechanisms, such as autapses of interneurons (Shi and Rayport, 1994; Tamás et al., 1997).

Second, because adaptation reflects the recent history of the neuron, it can serve as a means of temporal interaction between responses to different input signals that converge to a single neuron. Similar to the experimental observations on auditory neurons of the cricket (Pollack, 1988; Sobel and Tank, 1994), we show that when there is more than one signal present, the spike-frequency adaptation mechanism can help differentiate signals from two or several sources and produce selective responses only to the strongest input. It would be interesting to experimentally test whether such a forward masking effect, produced by intracellular calcium dynamics, takes place in cortical pyramidal neurons.

4.4. *Is Spike-Frequency Adaptation Present in Awake States?*

A major obstacle that has hindered our efforts to understand possible functional implications of spike-frequency adaptation, both in neuronal input-output computation and in emergent network dynamics, is our inability to assess its presence in cortical cells during awake behaving states of the brain. Most data on spike-frequency adaptation were obtained with *in vitro* slice preparations and *in vivo* intracellular recordings under anesthesia. These conditions are quite different from a wakeful state of the brain. It is well known that arousal is associated with activation of the brainstem system. Moreover, the I_{AHP} (and I_M) underlying spike-frequency adaptation are potently inhibited by neuromodulators released from the brainstem, such as acetylcholine, serotonin, and norepinephrine (Madison and Nicoll, 1984; McCormick and Williamson, 1989; Nicoll, 1988). On the other hand, adaptation was observed in intracellular recordings of neocortical pyramidal cells in awake cats (Baranyi et al., 1993a, 1993b), indicating that adaptation currents are likely to be present in awake states, with their amplitudes controlled and tuned by neuromodulators. Therefore, it would be of great interest to estimate quantitatively the strength of I_{AHP} in pyramidal neurons under various behavioral conditions. This would be feasible in practice, if the degree of cellular adaptation could be assessed from *extracellularly* recorded spike trains. Since the CC can be readily computed from spike trains, and its value is a monotonic function of g_{AHP} (Figs. 8B), it may provide a probe for assessing the strength of adapting ion currents (especially the I_{AHP}) under different *in vivo* conditions of the intact brain. Of course, negative temporal correlations in a spike train could also be caused by other mechanisms of delayed negative feedback, such as short-term synaptic depression or recurrent synaptic inhibition. These synaptic processes remain to be investigated. Since alternative processes have distinct time scales, their effects on the output's temporal structure should display characteristic frequency-dependence (such as in Fig. 8A), which may be used to distinguish one candidate mechanism from another.

To conclude, we would like to suggest that the serial coefficient of temporal correlation (*CC*) is as useful and important a characterization as the coefficient of variation (*CV*) for the ISIs of the neuronal output. Its experimental measurements and our understanding of its cellular and synaptic mechanisms could shed new insights into the dynamical operation of neurons in the cortex.

Appendix A: I_{AHP} Adaptation Model

The model is

$$C_m \frac{dV_m}{dt} = -g_L(V_m - V_{rest}) + C_m \Delta V \sum_i \delta(t - t_i) - g_{AHP}\,[Ca^{2+}]\,(V_m - V_K) \tag{24}$$

$$\frac{d[Ca^{2+}]}{dt} = -\frac{[Ca^{2+}]}{\tau_{Ca}}. \tag{25}$$

$$\text{If } V_m = V_{th}, \text{ then } \begin{cases} V_m \to V_{reset} \\ [Ca^{2+}] \to [Ca^{2+}] + \alpha. \end{cases} \tag{26}$$

The analysis will be carried out in the regime of sufficiently large input drive and high firing rates, when the noise effect is small. Therefore, in the following we replace the stochastic synaptic input by its mean current $I = C_m \Delta V \lambda$, where λ is the Poisson rate.

Because the dynamics of calcium is much slower than that of the membrane voltage, this model can be solved using the fast-slow variable analysis (Rinzel, 1985, 1987; Wang and Rinzel, 1995; Wang, 1998). The procedure consists of three steps.

In the first step, for the fast membrane dynamics $[Ca^{2+}]$ is first treated as if it was a constant parameter in Eq. (24). With $V = V_m - V_{reset}$ and $I_{eff} = I - g_L(V_{reset} - V_{rest})$, the model can be rewritten as

$$C_m \frac{dV}{dt} = -(g_L + g_{AHP}\,[Ca^{2+}])V + I_{eff} - g_{AHP}\,[Ca^{2+}]\,(V_{reset} - V_K). \tag{27}$$

$$\text{If } V = \theta, \text{ then } V \to 0, \tag{28}$$

with $\theta = V_{th} - V_{reset}$. Or

$$\frac{dV}{dt} = -\frac{V}{\tau_m^\star} + \frac{I^\star}{C_m}, \tag{29}$$

with

$$\frac{1}{\tau_m^\star} = \frac{1}{\tau_m} + \frac{g_{AHP}\,[Ca^{2+}]}{C_m} \tag{30}$$

$$I^\star = I_{eff} - g_{AHP}\,[Ca^{2+}]\,(V_{reset} - V_K). \tag{31}$$

If $I^\star$ and $\tau_m^\star$ are fixed, the solution for the firing rate of this integrate-and-fire model is

$$f = -\left[\tau_m^\star \ \ln\left(1 - \frac{C_m\theta}{I^\star\tau_m^\star}\right)\right]^{-1}. \tag{32}$$

Note that $I^\star$ and hence f are functions of I and $[Ca^{2+}]$.

In the second step, the slow calcium dynamics is considered, where the $[Ca^{2+}]$ influx is averaged over a firing cycle and becomes αf (the influx per spike times the instantaneous firing rate):

$$\frac{d[Ca^{2+}]}{dt} = \alpha f(I, [Ca^{2+}]) - \frac{[Ca^{2+}]}{\tau_{Ca}}. \tag{33}$$

Depending on whether the input is strong, $f(I, [Ca^{2+}])$ can be expanded linearly either by I (large I with strong input) or by $[Ca^{2+}]$ (low $[Ca^{2+}]$ level with weak input).

Strong Input Drive

With the assumption that $\frac{C_m\theta}{I^\star\tau^\star_m} \ll 1$ (for example, it is $0.075 \ll 1$ in our simulation), the firing rate can be expanded to the second order, yielding a linear relation between the firing rate and $I^\star$ as

$$f \simeq \frac{I^\star}{C_m\theta} - \frac{1}{2\tau_m^\star} = f_{init} - G_f[Ca^{2+}], \tag{34}$$

with

$$f_{init} = \frac{I_{eff}}{C_m\theta} - \frac{1}{2\tau_m} \tag{35}$$

$$G_f = \frac{g_{AHP}}{C_m}\left(\frac{V_{reset} - V_K}{\theta} + \frac{1}{2}\right). \tag{36}$$

Substituting f in Eq. (33) by Eq. (34), we obtain

$$\begin{aligned} \frac{d[Ca^{2+}]}{dt} &= \alpha f - \frac{[Ca^{2+}]}{\tau_{Ca}} \\ &= \alpha f_{init} - (\alpha G_f + 1/\tau_{Ca})\,[Ca^{2+}] \\ &= \alpha f_{init} - [Ca^{2+}]/\tau_{adap}, \end{aligned} \tag{37}$$

with

$$\tau_{adap} = \left[\frac{1}{\tau_{Ca}} + G_{adap}\right]^{-1}; \quad G_{adap} = \alpha G_f, \tag{38}$$

both are independent of the input amplitude.

Weak Input Drive, Low $[Ca^{2+}]$

When the input is not very strong, the linear relation between firing rate and $I^\star$ is no longer valid. Since the $[Ca^{2+}]$ level is low due to the low firing rate, we can analyze the system in the low $[Ca^{2+}]$ limit. The same Eq. (33) is expanded on small $[Ca^{2+}]$:

$$f \simeq f_{init} - G_f\,[Ca^{2+}], \tag{39}$$

with

$$f_{init} = -\left[\tau_m \ln\left(1 - \frac{C_m\theta}{I_{eff}\tau_m}\right)\right]^{-1} \quad (40)$$

$$G_f = \frac{b_0(I_{eff})g_L}{a_0(I_{eff})^2 C_m} - \frac{g_{AHP}}{a_0(I_{eff})C_m}, \quad (41)$$

and

$$a_0(I_{eff}) = -\ln\left(1 - \frac{g_L\theta}{I_{eff}}\right) \quad (42)$$

$$b_0(I_{eff}) = g_{AHP}\theta\frac{I_{eff} + g_L(V_{reset} - V_K)}{I_{eff}(I_{eff} - g_L\theta)}. \quad (43)$$

Therefore, we obtain the same equations as in case one Eqs. (37) and (38), except that f_{init} and G_f are now given by Eqs. (40) to (43). In the low $[Ca^{2+}]$ regime, the τ_{adap} is an increasing function of the input I_{eff} and approaches the input-independent value determined by Eq. (38) asymptotically with increasing input amplitude.

Finally, in the third step, by inserting the solution of the calcium equation into $f(I, [Ca^{2+}])$, the time evolution of the firing rate during adaptation process is solved.

The initial firing rate $f_{init} = f(I, [Ca^{2+}] = 0)$, or

$$f_{init} = -\left[\tau_m \ln\left(1 - \frac{C_m\theta}{I_{eff}\tau_m}\right)\right]^{-1}. \quad (44)$$

The steady-state $[Ca^{2+}]$ level is given by

$$\frac{d[Ca^{2+}]}{dt} = \alpha f - [Ca^{2+}]/\tau_{Ca} = \alpha f_{init} - \frac{[Ca^{2+}]}{\tau_{adap}} = 0, \quad (45)$$

which yield

$$[Ca^{2+}]_{ss} = \alpha\tau_{Ca} f_{ss} = \alpha\tau_{adap} f_{init}. \quad (46)$$

Thus,

$$F_{adap} \equiv \frac{f_{init} - f_{ss}}{f_{init}} = 1 - \frac{\tau_{adap}}{\tau_{Ca}}. \quad (47)$$

Substituting $1/\tau_{Ca} = 1/\tau_{adap} - G_{adap}$ in the above equation, we also obtain

$$F_{adap} = G_{adap}\tau_{adap}. \quad (48)$$

In summary, the dynamics of the system are

$$[Ca^{2+}](t) = [Ca^{2+}]_{ss}(1 - e^{-t/\tau_{adap}}) \quad (49)$$

$$f(t) = f_{ss} + (f_{init} - f_{ss})e^{-t/\tau_{adap}}. \quad (50)$$

Appendix B: Forward Masking

For clarity, we analyze the case when the strong and weak signals are evenly alternating as shown in Fig. 9B. The duration of each signal pulse $T = 100$ ms is the same as the time interval between pulses. The strength of the two inputs are λ_1 and λ_2. We define

$$I_i = \lambda_i \Delta V C_m - g_L(V_{reset} - V_{rest}) - \frac{C_m\theta}{2\tau_m}, i = 1, 2. \quad (51)$$

From Appendix A we know the steady-state $[Ca^{2+}]_i$ level is

$$[Ca^{2+}]_{i,ss} = \frac{\alpha\tau_{adap}}{C_m\theta} I_i. \quad (52)$$

The dynamics of $[Ca^{2+}]$ approaches $[Ca^{2+}]_{i,ss}$ during the signal pulse with time constant τ_{adap} and decays back to zero with time constant τ_{Ca} between input pulses. We denote the calcium level at the start and end point of signal i as $[Ca^{2+}]_{i,start}$ and $[Ca^{2+}]_{i,end}$:

$$\begin{cases} [Ca^{2+}]_{1,end} = (\alpha\tau_{adap}/C_m\theta)(1 - e^{-T/\tau_{adap}})I_1 \\ \qquad\qquad + e^{-T/\tau_{adap}}[Ca^{2+}]_{1,start} \\ [Ca^{2+}]_{2,start} = e^{-T/\tau_{Ca}}[Ca^{2+}]_{1,end} \\ [Ca^{2+}]_{2,end} = (\alpha\tau_{adap}/C_m\theta)(1 - e^{-T/\tau_{adap}})I_2 \\ \qquad\qquad + e^{-T/\tau_{adap}}[Ca^{2+}]_{2,start} \\ [Ca^{2+}]'_{1,start} = e^{-T/\tau_{Ca}}[Ca^{2+}]_{2,end}, \end{cases} \quad (53)$$

where $[Ca^{2+}]'_{1,start}$ is the $[Ca^{2+}]$ level at the beginning of the *next* cycle of the signal λ_1. In the steady state $[Ca^{2+}]'_{1,start} = [Ca^{2+}]_{1,start}$. Using this relation $[Ca^{2+}]_{1,start}$ and $[Ca^{2+}]_{2,start}$ can be solved from the above equation. In particular, the average starting calcium level is

$$[Ca^{2+}]_{start} = ([Ca^{2+}]_{1,start} + [Ca^{2+}]_{2,start})/2 = \kappa(I_1 + I_2), \quad (54)$$

where

$$\kappa = \frac{\alpha\tau_{adap}e^{-T/\tau_{Ca}}(1 - e^{-T/\tau_{adap}})}{2C_m\theta\left(1 - e^{-T(1/\tau_{Ca} + 1/\tau_{adap})}\right)}. \quad (55)$$

Since the fluctuation of $[Ca^{2+}]$ after the system reaches the steady state is small compared with $[Ca^{2+}]_{start}$, it is reasonable to treat the calcium level as a constant. We then obtain

$$f_i = \frac{1}{C_m \theta}[I_i - g_{AHP}[Ca^{2+}]_{start}\,(V_{reset} - V_K)]. \quad (56)$$

Finally, we obtain the response ratio

$$\frac{f_2}{f_1} = \frac{\rho(I_2/I_1) - 1}{\rho - (I_2/I_1)}, \quad (57)$$

where $\rho = 1/(g_{AHP}(V_{reset} - V_K)\kappa) - 1$ is independent of I_1 and I_2. For the parameter values used in Figs. 9 and 10, $\rho \simeq 4.3$. In Eq. (57) it is assumed that $I_2 > I_1$. The ratio f_2/f_1 diverges when $I_2/I_1 > \rho$, and the response to the smaller input is completely masked.

Acknowledgments

We thank L.F. Abbott, S. Seung, and C. van Vreeswijk for helpful comments on the manuscript. This work was supported by the National Institute of Mental Health (MH53717-01), the Alfred P. Sloan Foundation, and the W.M. Keck Foundation.

References

Abbott LF, van Vreeswijk C (1993) Asynchronous states in networks of pulse-coupled oscillators. *Phys. Rev. E* 48:1483–1490.

Ahmed B, Anderson JC, Douglas RJ, Martin KAC, Whitteridge D (1998) Estimates of the net excitatory currents evoked by visual stimulation of identified neurons in cat visual cortex. *Cerebral Cortex* 8:462–476.

Amit DJ, Tsodyks MV (1991) Quantitative study of attractor neural networks retrieving at low spike rates. *Network* 2:259–294.

Baranyi A, Szente MB, Woody CD (1993a) Electrophysiological characterization of different types of neurons recorded in vivo in the motor cortex of the cat. I. Patterns of firing activity and synaptic responses. *J. Neurophysiol.* 69:1850–1864.

Baranyi A, Szente MB, Woody CD (1993b) Electrophysiological characterization of different types of neurons recorded in vivo in the motor cortex of the cat. II. Membrane parameters, action potentials, current-induced voltage responses and electrotonic structures. *J. Neurophysiol.* 69:1865–1879.

Barkai E, Hasselmo ME (1994) Modulation of the input-output function of rat piriform cortex pyramidal cells. *J. Neurophysiol*. 72:644–658.

Brunel N (2000) Dynamics of sparsely connected networks of excitatory and inhibitory spiking neurons. *J. Comput. Neurosci*.

Calvin W, Stevens CF (1968) Synaptic noise and other sources of randomness in motoneuron interspike intervals. *J. Neurophysiol*. 31:574–587.

Connors BW, Gutnick MJ, Prince DA (1982) Electrophysiological properties of neocortical neurons in vitro. *J. Neurophysiol*. 48:1302–1320.

Douglas RJ, Koch C, Mahowald M, Martin KAC, Suarez HH (1995) Recurrent excitation in neocortical circuits. *Science* 269:981–985.

Ermentrout GB (1998) Linearization of F-I curve by adaptation. *Neural Comput*. 7:1721–1729.

Foehring R, Lorenzon NM, Herron P, Wilson CJ (1991) Correlation of physiologically and morphologically identified neuronal types in human association cortex in vitro. *J. Neurophysiol*. 65:1825–1837.

Gabbiani F, Koch C (1996) Coding of time-varying signals in spike trains of integrate-and-fire neurons with random threshold. *Neural Comput*. 8:44–66.

Guckenheimer J, Harris-Warrick R, Peck J, Willms A (1997) Bifurcation, bursting, and spike frequency adaptation. *J. Comput. Neurosci*. 4:257–277.

Hansel D, Mato G, Meunier C, Neltner L (1998) On numerical simulations of integrate-and-fire neural networks. *Neural Comput*. 10:467–484.

Helmchen F, Imoto K, Sakmann B (1996) Ca^{2+} buffering and action potential-evoked Ca^{2+} signaling in dendrites of pyramidal neurons. *Biophys. J*. 70:1069–1081.

Holden AV (1976) *Models of the Stochastic Activity of Neurones*. New York, Springer Verlag.

Holt GR, Softky WR, Koch C, Douglas RJ (1996) Comparison of discharge variability in vitro and *in vivo* in cat visual cortex neurons. *J. Neurophysiol*. 75:1806–1814.

Knight B (1972) Dynamics of encoding in a population of neurons. *J. Gen. Physiol*. 59:734–766.

Koch C (1999) *Biophysics of Computation*. New York, Oxford University Press.

Lancaster B, Zucker RS (1994) Photolytic manipulation of Ca^{2+} and the time course of slow, Ca^{2+}-activated K^+ current in rat hippocampal neurones. *J. Physiol. Lond*. 475:229–239.

Lapicque L (1907) Recherches quantitatives sur l'excitation électrique des nerfs traitée comme une polarisation. *J. Physiol. Pathol. Gen*. 9:620–635.

Lapicque L (1927) *L'excitabilité en fonction du temps*. Presses Universitaires de France, Paris.

Lorenzon NM, Foehring RC (1992) Relationship between repetitive firing and afterhyperpolarizations in human neocortical neurons. *J. Neurophysiol*. 67:350–363.

Madison DV, Nicoll RA (1984) Control of the repetitive discharge of rat CA1 pyramidal neurons *in vitro*. *J. Physiol*. 345:319–331.

Markram H, Helm PJ, Sakmann B (1995) Dendritic calcium transients evoked by single back-propagating action potentials in rat neocortical pyramidal neurons. *J. Physiol. Lond*. 485:1–20.

Mason A, Larkman A (1990) Correlations between morphology and electrophysiology of pyramidal neurons in slices of rat visual cortex. *J. Neurosci*. 10:1415–1428.

McCormick DA, Connors BW, Lighthall JW, Prince DA (1985) Comparative electrophysiology of pyramidal and sparsely spiny stellate neurons of the neocortex. *J. Neurophysiol*. 54:782–805.

McCormick DA, Williamson A (1989) Convergence and divergence of neurotransmitter action in human cerebral cortex. *Proc. Natl. Acad. Sci. USA* 86:8098–8102.

Nicoll RA (1988) The coupling of neurotransmitter receptors to ion channels in the brain. *Science* 241:545–551.

Pollack GS (1988) Selective attention in an insect auditory neuron.

J. Neurosci. 8:2635–2639.

Press WH, Flannery BP, Teukolsky SA, Vetterling WT (1989) *Numerical Recipes*. Cambridge University Press, Cambridge.

Ricciardi LM (1977) *Diffusion Processes and Related Topics in Biology*. Springer-Verlag, Berlin.

Rieke F, Warland D, de Ruyter van Steveninck R, Bialek W (1997) *Spikes: Exploring the Neural Code*. MIT Press, Cambridge, MAS.

Rinzel J (1985) Bursting oscillations in an excitable membrane model, in ordinary and partial differential equations. *Lecture Notes in Mathematics*. Springer, New York. vol. 1151, pp. 304–316.

Rinzel J (1987) A formal classification of bursting mechanisms in excitable systems. In: Gleason, AM, ed. *Proceedings of the International Congress of Mathematicians*. American Mathematical Society, Providence, RI. pp. 1578–1594.

Schiller J, Helmchen F, Sakmann B (1995) Spatial profile of dendritic calcium transients evoked by action potentials in rat neocortical pyramidal neurones. *J. Physiol*. 487(3):583–600.

Shadlen MN, Newsome WT (1994) Noise, neural codes and cortical organization. *Curr. Opin. Neurobiol*. 4:569–579.

Shi WX, Rayport S (1994) GABA synapses formed *in vitro* by local axon collaterals of nucleus accumbens neurons. *J. Neurosci*. 14:4548–4560.

Sobel EC, Tank DW (1994) In vivo Ca^{2+} dynamics in a cricket auditory neuron: An example of chemical computation. *Science* 263:823–826.

Softky WR (1995) Simple codes versus efficient codes. *Curr. Opin. Neurobiol*. 5:239–247.

Softky WR, Koch C (1993) The highly irregular firing of cortical cells is inconsistent with temporal integration of random EPSPs. *J. Neurosci*. 13:334–350.

Somers D, Nelson S, Sur M (1995) An emergent model of orientation selectivity in cat visual cortical simple cells. *J. Neurosci*. 15:5448–5465.

Stein RB (1965) A theoretical analysis of neuronal variability. *Biophys. J*. 5:173–195.

Stein RB (1967) Some models of neuronal variability. *Biophys. J*. 7:37–68.

Stemmler M, Usher M, Niebuhr E (1995) Lateral interaction in primary visual cortex: A model bridging physiology and psychophysics. *Science* 269:1977–1880.

Svoboda K, Denk W, Kleinfeld D, Tank D (1997) In vivo dendritic calcium dynamics in neocortical pyramidal neurons. *Nature* 385:161–165.

Tamás G, Buhl EH, Somogyi P (1997) Massive autaptic self-innervation of GABAergic neurons in cat visual cortex. *J. Neurosci*. 17:6352–6364.

Traub RD (1982) Simulation of intrinsic bursting in CA3 hippocampal neurons. *Neurosci*. 7:1233–1242.

Treves A (1993) Mean-field analysis of neuronal spike dynamics. *Network* 4:259–284.

Troyer TW, Miller KD (1997) Physiological gain leads to high *ISI* variability in a simple model of a cortical regular spiking cell. *Neural Comput*. 9:971–983.

Tuckwell H (1988) *Introduction to Theoretical Neurobiology*. Cambridge University Press, Cambridge. vol. 2.

van Vreeswijk C, Sompolinsky H (1996) Chaos in neuronal networks with balanced excitatory and inhibitory activity. *Science* 274:1724–1726.

Wang XJ (1998) Calcium coding and adaptive temporal computation in cortical pyramidal neurons. *J. Neurophysiol*. 79:1549–1566. Corrigendum, *J. Neurophysiol*. 79 (March 1998).

Wang XJ, Rinzel J (1995) Oscillatory and bursting properties of neurons. In: Arbib MA, ed. *The Handbook of Brain Theory and Neural Networks*. MIT Press, Cambridge, MA. pp. 686–691.

Wax N, ed. (1954) *Selected Papers on Noise and Stochastic Processes*. Dover, New York.